# Dynamics of charge current gratings generated in GaAs by ultrafast quantum interference control

Y. Kerachian, P. A. Marsden, and H. M. van Driel*
*Department of Physics and Institute for Optical Sciences, University of Toronto, Toronto, Canada M5S1A7*

Arthur L. Smirl
*Laboratory for Photonics and Quantum Electronics, 138 IATL, University of Iowa, Iowa City, Iowa 52242, USA*
(Received 21 July 2006; revised manuscript received 9 January 2007; published 19 March 2007)

Ballistic charge current gratings are induced in GaAs at 300 K by quantum interference of single- and two-photon absorption using noncollinearly incident 775 and 1550 nm, 150 fs pulses. First-order diffraction of time-delayed 830 nm, 150 fs probe pulses is used to observe carrier evolution for injected densities near $10^{17}$ cm$^{-3}$. The current grating forms electron and hole charge-density gratings during pumping, and because the pumping is uniform while the carrier density and hence electronic specific heat is not, a carrier temperature grating also forms. The peak diffraction efficiency from both grating types is only $\sim 10^{-9}$. The temperature grating, with modulation amplitude $\sim 1$ K, decays through cooling in $\sim 500$ fs. Space-charge fields neutralize the electron and hole density gratings by the end of pumping, but nonetheless leave a neutral, electron-hole pair density grating with amplitude of $\sim 10^{-3}$ of the injected carrier density. At the highest injected carrier densities, the pair grating amplitude builds on a few picosecond time scale before decaying by recombination and ambipolar diffusion with an $\sim 15$ ps time constant. A model based on continuity equations for carrier density, momentum, and energy during ballistic and drift motion is used to help interpret the experimental data. Besides qualitatively confirming the above dynamics, the model suggests that the pair grating amplitude and evolution is determined by two factors: (1) the warping or nonparabolicity of the hole bands and (2) the transfer of some electrons from the $\Gamma$-valley electron-density grating to the $L$, $X$ conduction band valleys during excitation, and their subsequent return to the $\Gamma$ valley on a few picosecond time scale.

DOI: 10.1103/PhysRevB.75.125205 PACS number(s): 78.47.+p, 72.20.Ht, 42.65.−k

## I. INTRODUCTION

The ultrafast dynamics of photoexcited carriers in bulk and low-dimensional semiconductors have been extensively studied using short pulse laser sources.[1] Carrier thermalization, scattering, cooling, recombination, etc., are now reasonably well understood in many bulk and quantum well materials. The experiments to observe such behavior were typically designed to excite and probe spatially homogeneous electrons and holes, although degenerate four-wave mixing experiments have also been employed to induce interband polarization or density gratings to study, e.g., anisotropic state filling[2] on a 100 fs time scale, or carrier diffusion, recombination, and photorefractive behavior on a longer time scale.[3] Ballistic or drift charge motion is usually not induced or considered and, if so, is related to applied dc electric or magnetic fields.

In recent years, it has been shown that phased optical beams can be used without any external bias to generate ballistic pure charge or spin-polarized charge currents,[4–8] and pure spin currents[9,10] in bulk, direct gap semiconductors via valence-conduction-band transitions. Charge currents have also been produced in semiconductor quantum wells or doped materials via discrete states.[11–15] Current generation is based on quantum interference control[16] (QUIC), involving the interference of absorption pathways connecting the same initial and final states for one or more optical perturbations. For semiconductors with cubic symmetry, charge current injection requires a two-color process with interference occurring between single- and two-photon transition amplitudes[4] involving photons of energies $2\hbar\omega$ and $\hbar\omega$, respectively, with $\hbar\omega < E_g < 2\hbar\omega$, where $E_g$ is the fundamental band gap. This two-color QUIC scheme is shown in Fig. 1(a) wherein harmonically related beam components couple the same valence- and conduction-band states. The relative phase and polarization of the optical beams, as well as the symmetry of the material, govern the current injection magnitude and direction.

In most previous two-color QUIC experiments, the optical pulses were incident collinearly and phase control was typically obtained with a scanning Michelson interferometer. If, however, the pulses are noncollinearly incident on a semiconductor wafer, the phase of the optical beams varies in the plane of the material, inducing transient, spatial current gratings. Noncollinear QUIC processes were used earlier[17] to generate pure electron spin current gratings in GaAs at 300 K using 775 and 1550 nm, *orthogonally* polarized 150 fs pulses. The spin current grating evolves into a pure spin population grating (with no carrier density modulation) and is observed to decay by electron spin diffusion on a 3 ps time scale from the measurements of diffracted 830 nm probe pulses.

Here, we use the same noncollinear two-color excitation and 830 nm probing scheme, but with *parallel-polarized* pump pulses. This configuration leads to ballistic, spin-unpolarized charge current gratings in GaAs. The subsequent carrier evolution is much more complex than that following spin current injection as the transport changes from a ballistic to a diffusive regime. Initially, the current grating produces electron and hole charge density gratings of different

 

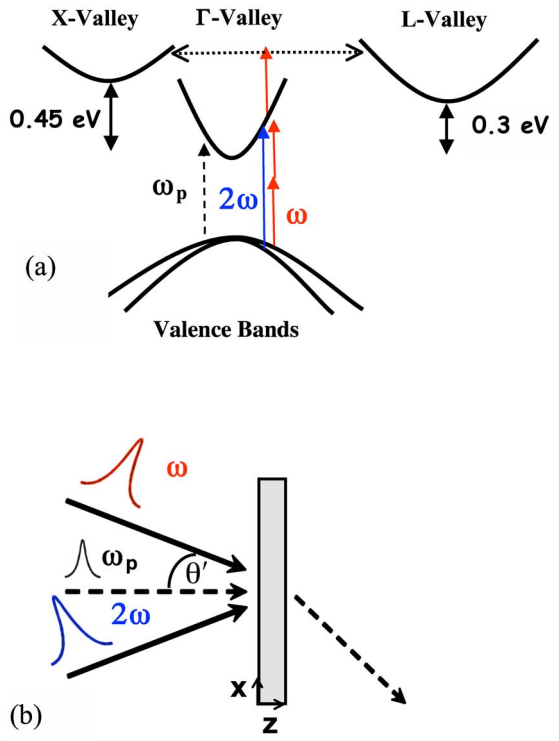


FIG. 1. (Color online) (a) Schematic electron band picture associated with production of a transient charge current by pump pulses with frequencies $\omega$ and $2\omega$ also illustrated is free-carrier absorption of electrons into higher $X$, $L$ valleys, and probing with pulses of frequency $\omega_p$. (b) Geometry for transient grating experiments with grating evolution monitored by a diffracted probe pulse.

amplitudes. Due to a space-charge coupling field, the carriers move into a neutral, electron-hole pair population grating (hereafter simply called a "pair grating") during the pulse. Subsequently, the pair grating decays with a 15 ps time constant by ambipolar diffusion and carrier recombination. Because a carrier density grating forms during the optical pulse, the carrier specific heat is also modulated. As the optical energy is uniformly deposited into the carriers, and with carrier cooling also occurring, a carrier temperature grating is formed. The temperature grating amplitude relaxes as the carrier temperature approaches the lattice temperature with a 500 fs time constant. During optical pumping, the 1550 nm beam also transfers by free-carrier absorption some electrons, including those forming an electron charge density grating, to the heavy mass $L$ or $X$ conduction bands [see Fig. 1(a)]. When these electrons return to the $\Gamma$ valley, they increase the pair grating efficiency within a few picoseconds before decaying occurs via recombination and/or diffusion.

Much of the information obtained here might be difficult to access via other techniques such as standard pump-probe differential transmission of carrier distributions. Unlike differential transmission, transient diffraction is a background-free technique, allowing one to observe extremely small variations in carrier population and temperature. For current induced gratings, the amplitude of the grating is related to the distance the carriers move. As will be shown below, one can detect carrier displacements in the nanometer range, much less than the grating period, which is related to the optical wavelength. Density grating amplitudes of only $\sim 10^{14}$ cm$^{-3}$ and carrier temperature gratings of amplitude of $\sim 1$ K, with diffraction efficiency of $\sim 10^{-10}$, are observable.

To help us qualitatively interpret the experimental results, we have used a model for the carriers' ballistic and drift motion and decay through momentum relaxation and space-charge fields. Interestingly, in addition to confirming the above picture for the grating evolution, the results suggest that while the peak electron and hole density grating amplitudes depend on the *ballistic velocity* by which electrons and holes are injected, the amplitude and the phase of the pair grating that survive after ballistic motion ceases are governed by the warping or nonparabolicity of the hole band.

The remainder of this paper is organized as follows. We first provide the essential elements of how two-color QUIC processes can lead to charge current gratings and briefly describe diffraction grating probing. In Sec. III, we provide experimental details on the experimental techniques and data related to charge current injection in GaAs at 300 K and evolution of the current grating into carrier temperature and charge density gratings, followed by pair grating formation. The simple model for the carriers' quasiballistic and drift motion is presented along with a discussion of the influence of relevant semiconductor parameters on the formation of the different types of gratings. Finally, we offer a summary of the key features observed.

## II. THEORETICAL BACKGROUND

### A. Grating formation

The basic geometry used for the generation of a transient charge current grating by nominally 150 fs pulses is illustrated in Fig. 1(b). Two noncollinear, linearly polarized pump pulses with frequencies $\omega$ and $2\omega$, which excite electrons from the heavy and light hole valence bands to the conduction band via two-photon and single-photon absorption, as shown in Fig. 1(a), are incident on a noncentrosymmetric semiconductor crystal depicted in Fig. 1(b). If the pulses are colinearly polarized, QUIC charge currents are generated in the polarization direction, with the current amplitude only weakly dependent on crystal orientation.[4] The complex electric fields for the pump pulses can be written as a function of position $\mathbf{r}$ and time $t$ as

$$\boldsymbol{E}_{\omega}(\boldsymbol{r},t) = E_{\omega}(t)\hat{\boldsymbol{e}}_{\omega}\exp(-i\omega t + i\boldsymbol{k}_{\omega}\cdot\boldsymbol{r} + i\phi_{\omega}),$$

$$\boldsymbol{E}_{2\omega}(\boldsymbol{r},t) = E_{2\omega}(t)\hat{\boldsymbol{e}}_{2\omega}\exp(-2i\omega t + i\boldsymbol{k}_{2\omega}\cdot\boldsymbol{r} + i\phi_{2\omega}), \quad (1)$$

where $\boldsymbol{k}_{\omega,2\omega}$, $\hat{\boldsymbol{e}}_{\omega,2\omega}$, and $E_{\omega,2\omega}(t)$ are the propagation vector, polarization vector, and envelope of the $\omega$ and $2\omega$ pulses inside the material.

The injected current density $\boldsymbol{J}$ depends on the optical electric fields and a fourth-rank current injection tensor[4] $\vec{\vec{\eta}}$. For photon energies not large enough to excite carriers from the spin-orbit split-off band, current contribution can come from carriers in light and heavy holes as well as the conduction band near the $\Gamma$ point so that $\vec{\vec{\eta}}=\Sigma_c\vec{\vec{\eta}}_c$ for $c=\Gamma$, hh, and lh, and the current injection rate is given by

$$\dot{J} = \sum_c \dot{J}_c = \sum_c \vec{\eta}_c : \boldsymbol{E}_\omega \boldsymbol{E}_\omega \boldsymbol{E}^*_{2\omega} + \text{c.c.}. \tag{2}$$

In the experiments described below, 1550 ($\omega$) and 775 nm ($2\omega$) pulses are incident on a (001) surface of a cubic semiconductor (GaAs) with the $\omega(2\omega)$ pulse's propagation vector making an angle *outside* the material of $\theta' = 10°(-10°)$ with the [001] crystal axis, which we define as the **z** axis. The pump pulses are taken to be $p$ polarized in the plane containing [100] and [001] axes with polarization vectors *within* the material of $\hat{\boldsymbol{e}}_{\omega,2\omega} = \hat{\boldsymbol{x}} \cos\theta \pm \hat{\boldsymbol{z}} \sin\theta$, where [100] defines an **x** axis and $\theta \approx \theta'/n$ for small angles, with $n$ being the refractive index. The propagation vectors within the material are given by $\boldsymbol{k}_{\omega,2\omega} = |\boldsymbol{k}_{\omega,2\omega}|(\mp\hat{\boldsymbol{x}} \sin\theta + \hat{\boldsymbol{z}} \cos\theta)$. If the semiconductor is optically thin, propagation and/or dispersion effects can be ignored with absorption occurring uniformly throughout the material. Hence, current generation can be considered to be one dimensional with any system variable only depending on $x$. The injection rate of charge current density along the $x$ axis takes the form of a grating given by

$$\dot{J}^x = 2\,\text{Im}(\eta^{xxxx}) E^x_\omega E^x_\omega E^x_{2\omega} \sin(K_g x), \tag{3}$$

where $K_g = 2\pi/\Lambda_g = (2k_\omega + k_{2\omega}) \sin\theta$ is the grating wave number for grating period $\Lambda_g$ and the origin for the $x$ axis is chosen to eliminate the constant phases $\phi_{\omega,2\omega}$ of Eq. (1). The tensor element in Eq. (3) is the largest[4,18] of the four distinguishable nonzero elements, although the largest currents [~30% larger than indicated by Eq. (3)] are obtained for beams polarized along the [111] direction [but not accessible for a (001) surface]. Following earlier descriptions,[4] we define an average (or "swarm") velocity with which carriers are injected $u^s_c$ via $\dot{J}^x_c = \mp e u^s_c \sin(K_g x) (\partial N_c/\partial t)|^{inj}$, where $N_c$ is the density of carrier $c$, with the $(-)$ sign relating to electrons and the $(+)$ sign to holes. The swarm velocities reflect the fact that carriers are injected into a polar distribution in momentum space; typically, the swarm velocity is much less than an individual carrier's group velocity since only a fraction of the injected carriers have a directed motion, or, stated differently, the $x$ component of the net velocity of all carriers of a given type is less than an individual carrier's group velocity.

In Fig. 2(a), we schematically illustrate the charge current grating in the case where electrons and holes move in opposite directions, the case for collinearly polarized optical pulses. Figure 2(b) shows the electron and hole population gratings that subsequently form. Space-charge fields act to remove the spatial charge imbalance, with charge neutrality occurring within the dielectric relaxation time.[19] For an electron-hole carrier density of $\sim 10^{17}$ cm$^{-3}$, this time is only a few femtoseconds so that local charge neutrality should occur by the end of ~100 fs pump pulses. As Fig. 1(a) suggests, the 1550 nm (0.8 eV) pump pulse can also transfer some of the $\Gamma$-valley electrons (including those contributing to the density grating) via free-carrier absorption[20] to the six $L$ or four $X$ valleys, which are located[21,22] $\Delta_L = 0.3$ eV and $\Delta_X = 0.45$ eV above the $\Gamma$-valley minimum. These electrons return to the $\Gamma$ valley within[23] a few pecoseconds where they can influence the transmission and diffraction properties of the probe beam. The pair grating, illustrated in Fig. 2(c), is expected to decay on a time scale related to ambipolar diffusion and recombination.

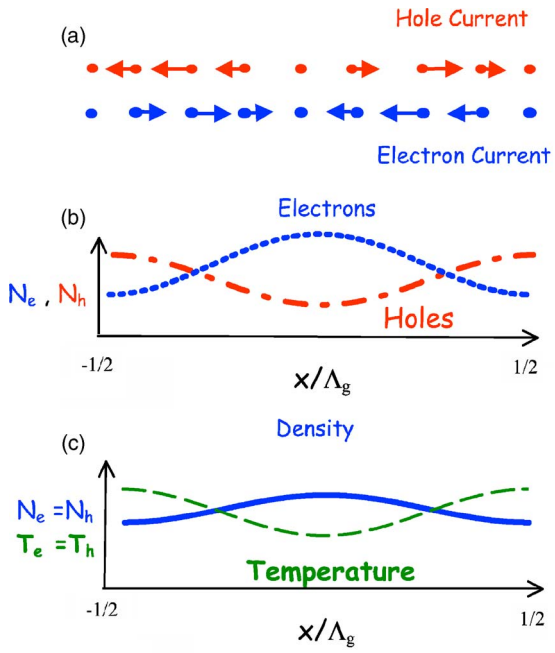


FIG. 2. (Color online) Schematic of grating formation. (a) Illustrates the spatially varying injected electron and hole currents over one period, (b) indicates the carrier charge density gratings that are subsequently formed, while (c) shows that the grating indicated in (b) evolves into a neutral electron-hole density grating and produces a carrier temperature grating.

The formation of electron or hole density gratings during the optical pulse [Fig. 2(b)] implies that the electron-hole specific heat is also modified, as Fig. 2(b) suggests. Hence, as electron-hole pairs and their excess energy $2\hbar\omega - E_g$ are deposited in a spatially uniform fashion by the pump pulses, and because these carriers lose energy to the lattice during the excitation period, a carrier temperature grating develops, as illustrated in Fig. 2(c). This grating is expected to decay by carrier cooling to the lattice temperature with a time constant of[1] ~500 fs. As the $(L,X)$ valley electrons return from the side valleys within a few picoseconds, they only weakly moderate this cooling rate.

### B. Grating probing

Carrier density and temperature gratings produce a grating in Fermi occupancy factors and hence a grating in a probe absorption coefficient and possibly also in the refractive index. The absorption coefficient for an interband probe beam [see Fig. 1(a)] at frequency $\omega_p$ can be expressed[24] as $\alpha = \Sigma_v\, \alpha_v[1 - f_\Gamma(E_v) - f_v(E_v)]$, where the summation is over hh and lh valence bands from which electrons can be excited and $f_{\Gamma,v}(E_v)$ are the electron or hole Fermi occupancy factors evaluated at the appropriate $\Gamma$-electron or hole energies for states optically coupled by the probe beam. For GaAs,[25] $\alpha_{hh} \approx 2/3\alpha_0$ and $\alpha_{lh} \approx 1/3\alpha_0$, where[22] $\alpha_0$ is the quiescent absorption coefficient of the probe pulse. For our probe wave-

length, the Pauli blocking factor is dominated[24] by $f_\Gamma(E_{\rm lh})$. Note that diffraction techniques cannot directly detect charge current gratings since probe absorption is not sensitive to carrier macroscopic motion, but rather the distribution function itself.

Because of the spatial periodicity of the carrier system, any system variable can be expressed as a Fourier series. In particular, for any band $c$, the average carrier velocity $u_c$, carrier density $N_c$, carrier temperature $T_c$, and space-charge field $E$ take the form

$$u_c(x,t) = \sum_{m=1,2,\ldots} u_c^{(m)}(x,t)\sin K_m x,$$

$$N_c(x,t) = \sum_{m=0,1,\ldots} N_c^{(m)}(t)\cos K_m x,$$

$$T_c(x,t) = \sum_{m=0,1,\ldots} T_c^{(m)}(t)\cos K_m x,$$

$$E(x,t) = \frac{e}{\varepsilon}\int_0^x [N_h(x') - N_e(x')]dx'$$

$$= \frac{e}{\varepsilon}\sum_{m=1,2,\ldots} (K_m)^{-1}[N_h^{(m)}(t) - N_e^{(m)}(t)]\sin K_m x, \quad (4)$$

where $K_m = mK_g$, $\varepsilon$ is the effective dielectric constant of the semiconductor wafer, and $N_h = N_{\rm hh} + N_{\rm lh}$ and $N_e = N_\Gamma + N_{L,X}$ are total hole and electron densities. The time dependence of the variables resides entirely in the Fourier, or grating, amplitudes. Similarly, we have $f_c(x,t) = \Sigma_{m=0,1,..} f_c^{(m)}(t)\cos mK_g x$. For the $m \neq 0$ coefficients and, e.g., the $\Gamma$-valley electrons, one has

$$f_\Gamma^{(m)} = N_\Gamma^{(m)} \left.\frac{\partial f_\Gamma}{\partial N_\Gamma}\right|_{T_\Gamma} + T_\Gamma^{(m)} \left.\frac{\partial f_\Gamma}{\partial T_\Gamma}\right|_{N_\Gamma} \quad (5)$$

for small $N_\Gamma^{(m)}$ and $T_\Gamma^{(m)}$. From Eq. (5), one can obtain the absorption, grating amplitudes, $\alpha^{(m)}$ and, with the aid of the Kramers-Kronig relations,[24] the associated refractive index grating amplitude $n^{(m)}$. The first-order diffraction efficiency of a thin grating is given by[26]

$$\zeta = e^{-\alpha_0 L}\frac{L^2}{4}\left[(k_{pr}n^{(1)})^2 + \left(\frac{1}{2}\alpha^{(1)}\right)^2\right], \quad (6)$$

where $k_{pr}$ is the probe beam vacuum propagation constant and $L$ is the semiconductor thickness. For our experimental parameters, the index grating makes a much smaller[25] contribution than the absorption grating and will not be considered further.

## III. EXPERIMENTAL RESULTS AND ANALYSIS

### A. Methodology

The sample used for the experiments, which are all carried out at 300 K, is an $L$=790-nm-thick (001)-grown bulk GaAs sample that is antireflection coated for 800 nm light and mounted on a glass substrate. The 1550 nm pulses ($\omega$ pulses) are produced by an optical parametric amplifier (OPA) that is pumped by a regeneratively amplified Ti:sapphire laser operating at 250 kHz. The second harmonic of these pulses, with a carrier wavelength of 775 nm ($2\omega$ pulses), is produced by frequency doubling of $\omega$ pulses in a beta barium borate (BBO) crystal. The $\omega$ and $2\omega$ pump pulses, which have full width at half maximum (FWHM) widths of ~150 fs, are $p$ polarized along the crystal [100] direction and are temporally and spatially overlapped on the sample with $\theta' = \pm 10°$, giving induced current gratings with $\Lambda_g = 2.2$ $\mu$m. The $\omega$ and $2\omega$ beams have focal spot sizes (FWHM) of 60 and 110 $\mu$m, respectively. The $2\omega$ and $\omega$ pump peak incident intensities are varied up to ~140 MW cm$^{-2}$ and ~5 GW cm$^{-2}$, respectively, for which each pulse would independently generate in the sample average carrier densities of $\sim 5\times 10^{17}$ and $\sim 1\times 10^{17}$ cm$^{-3}$, respectively. The absorption depth[22] of the 775 nm beam (0.7 $\mu$m) is 0.7 $\mu$m, comparable to sample thickness. Measurements of the pump transmission as a function of 775 nm intensity indicate that deviations from linearity due to Pauli blocking become significant for incident intensities >30 MW cm$^{-2}$.

A third, time-delayed probe pulse with a carrier wavelength of 830 nm obtained by splitting off a portion of the output of the regenerative amplifier is normally incident on the grating; the quiescent probe absorption coefficient is $\alpha_0 = 0.9\times 10^4$ cm$^{-1}$. The $s$-polarized probe pulses (i.e., polarized along the [010] crystal direction) are focused at near-normal incidence to a spot size of ~40 $\mu$m onto the center of the pump beams' spot; the focused probe peak intensity is ~10 MW cm$^{-2}$. The first-order diffracted signal is measured using a photomultiplier appropriately positioned behind the GaAs sample. When this signal is divided by the incident intensity, the diffraction efficiency $\zeta$ is obtained.

By also measuring the (undiffracted) transmission of the probe beam with ($T'$) and without ($T$) one or both pump pulses present, we are also able to determine the differential transmission $\Delta T/T = (T' - T)/T$ for different pumping conditions. For our pumping and probing wavelengths and injected carrier densities,[24] $\Delta T/T \approx \alpha_{\rm lh} L f_\Gamma(E_{\rm lh})$.

### B. Experimental results

We first present and discuss the experimental results for the time-resolved transmission and diffraction experiments and defer detailed interpretation to the following section. Figure 3 shows the (undiffracted) time-dependent differential probe transmission, $\Delta T/T$, for two different pumping conditions. Figure 3(a) depicts data for which an ~70 MW cm$^{-2}$, 775 nm pump pulse alone is present, while Fig. 3(b) displays corresponding data for 70 MW cm$^{-2}$, 775 nm and 5 GW cm$^{-2}$, 1550 nm pump pulses. For the 775 nm pump pulse alone, $\Delta T/T$ rises to its peak value within ~250 fs, while Fig. 3(b) shows a similar fast rise-time component with an additional component with a rise time of ~5 ps. The initial fast rise in both cases approximately follows the integral of the excitation pulse envelope and principally reflects increasing Pauli blocking the probe pulse encounters with increasing carrier density. The 775 nm data suggest that the

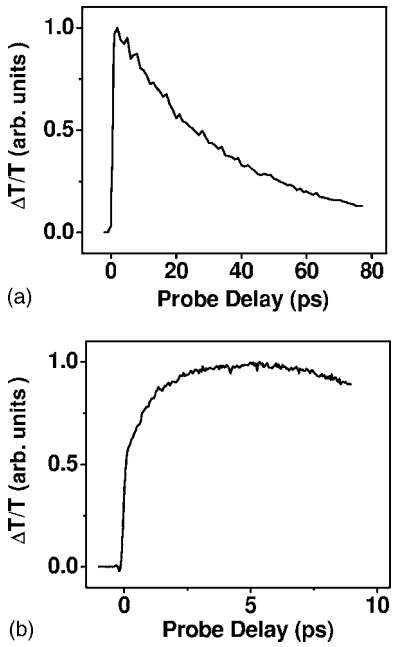


FIG. 3. Measured differential probe transmission of 830 nm, 150 fs probe pulses as a function of time delay from 775, 1550 nm pump pulses under various pumping conditions. (a) For ~70 MW cm$^{-2}$, 775 nm peak intensity pump pulse; (b) same as (a) but with a 5 GW cm$^{-2}$, 1550 nm pump pulse also incident.

thermalization of these carriers, or at least their transfer, into the probed electron states (which lie lower than those into which electrons are injected) is of the order of (or shorter than) the pulse width. The slower rise component observed in Fig. 3(b) likely reflects an increase in the occupancy of the probed states due to (i) the relaxation of carriers as they cool or (ii) an increase in the carrier density together with a slowing of the Γ-electron cooling as the higher-energy carriers, initially deposited in the side $L$, $X$ valleys by free carrier absorption of 1550 nm photons, return to the Γ valley with a 2.5 ps time constant.[23] It may also be possible that at the highest pump intensities, (iii) hot phonon effects[27] slow the cooling rate. For both Figs. 3(a) and 3(b), the decrease in $\Delta T/T$ beyond 5 ps is indicative of nonradiative recombination with a characteristic time of ~36 ps. Recombination times between 30 and 50 ps are measured, depending on illumination spot, indicating that the recombination is likely due to surface defects. This variation was also observed in earlier work that dealt with spin current gratings.[17]

Figure 4(a) shows the time-dependent diffraction efficiency $\zeta$ for 2 GW cm$^{-2}$, 1550 nm and 17 MW cm$^{-2}$, 775 nm noncollinearly incident pulses. Figures 4(b) and 4(c) show similar data for 5 GW cm$^{-2}$, 1550 nm and 140 MW cm$^{-2}$, 775 nm pump pulses. The peak diffraction efficiency (near zero time delay) in the latter case is $(5\pm2)\times10^{-9}$, indicating how weak the gratings are. In both cases, the grating efficiency rises rapidly with the pump pulses and then decays to a nonzero level with a characteristic time of ~0.5 ps, a time not limited by the pump pulse widths as indicated by the displayed cross-correlation function of the pump and probe pulses. The peak of the diffracted signal is time shifted relative to the autocorrelation trace, with the

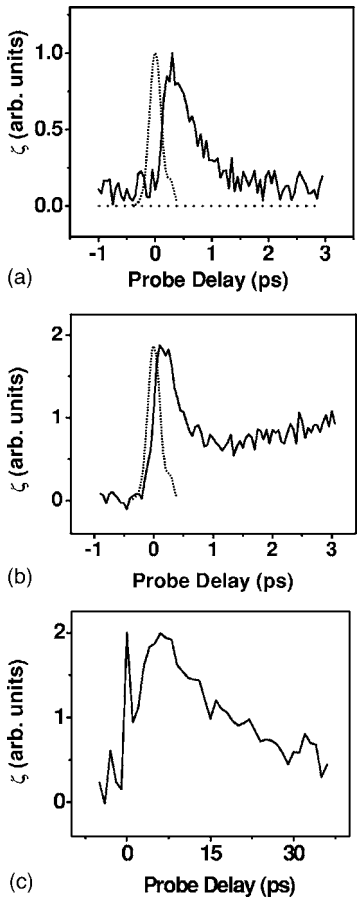


FIG. 4. (a) Measured first-order grating diffraction efficiency $\zeta$ of 830 nm, 150 fs probe pulses as a function of time delay from 17 MW cm$^{-2}$, 775 nm and 2 GW cm$^{-2}$, 1550 nm pump pulses incident on GaAs at 300 K. The dotted curve indicates the cross-correlation function of the pump and probe pulses. (b) Similar data as in (a) but for 140 MW cm$^{-2}$, 775 nm and 5 GW cm$^{-2}$, 1550 nm pump pulses. (c) Same as (b) but for a longer time scale.

displacement more noticeable at the lower pumping intensities. While part of this shift may be related to measurement uncertainty, an actual shift is not unexpected since the density grating amplitude (and possibly the temperature grating amplitude) does not necessarily peak with the pump pulses. With increasing pump intensity and carrier density, space-charge effects will reduce this delay as will a shorter carrier thermalization time, which allows electrons to more quickly fill the states to which the probe pulse is sensitive. For the higher intensity pump pulses, $\zeta$ shows a second peak at ~4–5 ps before decaying with a 15±4 ps time. We defer the discussion of the grating evolution for probe delays <5 ps until we present a model for the carrier evolution below, but one can understand the ~15 ps decay time in terms of ambipolar diffusion and recombination. The decay rate for the pair grating diffraction efficiency is given by[3] $2(K_g^2 D_a + \gamma_R)$, where $D_a$ is the ambipolar diffusion constant and $\gamma_R$ is the carrier recombination rate. From Fig. 3, we determined $\gamma_R$ ~0.03 ps$^{-1}$. From the measured[22,28] $D_a$=20 cm$^2$ s$^{-1}$ for our peak density, one would expect a grating decay time of 12 ps, consistent with the value obtained from the data in Fig. 4(c).

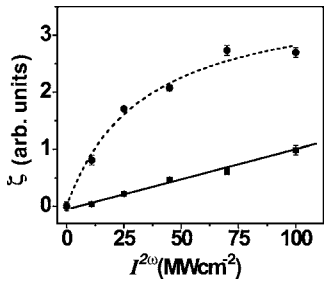


FIG. 5. Measured diffraction efficiency $\zeta$ of probe pulse as a function of 775 nm beam incident intensity with the 1550 nm pulse intensity adjusted to produce the same number of electron-hole pairs: (a) at peak, near zero time delay (circles) and (b) at 4 ps time delay (squares). The dotted and solid curves are guides to the eye.

Figure 5 shows the variation of the peak value of $\zeta$ (near zero time delay) and at ~4 ps delay as a function of the 775 nm pulse incident intensity. For these measurements, the intensity of the 1550 nm pulse is also varied so that both pulses generate approximately the same number of carriers, i.e., the 1550 nm pulse intensity is doubled when the 775 pulse intensity is quadrupled. Near zero time delay $\zeta$ shows sublinear behavior for 775 nm beam intensity $>25$ MW cm$^{-2}$, while at 4 ps delay $\zeta$ varies nearly linearly with 775 nm beam intensity. A possible origin for the difference in the two behaviors is discussed in terms of the model below.

### C. Grating evolution model

To provide further insight into the experimental results and the role that various mechanisms might have during the complex dynamics, we consider a simple model for the current dynamics. Our goal is modest in that we only hope to provide *qualitative* insight into some of the underlying physical processes. Carriers generated by subpicosecond pulses are initially in a highly nonequilibrium state, and the development of a model to deal with all aspects of carrier current, density, and energy evolution is challenging[1,14,29] and beyond the scope of this paper. We focus on modeling the carrier density, momentum, and temperature in the quasiballistic current regime following carrier injection in the drift regime, where the carriers respond to a space charge field, and during the time that carriers come to thermal equilibrium with the lattice. Because of the model's simplicity, no attempt is made to quantitatively fit simulation results to the experimental data. Known parameters (see Table I) for GaAs are used in the modeling and we simply calculate what such a model, with its various assumptions, gives. A more sophisticated model would likely incorporate, *inter alia*, carrier dynamics in momentum ($\vec{k}$) space including separation of coherently and incoherently moving carriers, many-body effects (e.g., band-gap renormalization, screening, etc.) for high carrier density, and non-Boltzmann distribution function. However, because of data limitations (signal-to-noise ratio, spatial and temporal convolution effects, etc.), this more sophisticated approach is not justified here; indeed, such a model would introduced additional parameters whose fitted values would be increasingly questionable.

TABLE I. GaAs parameters at 300 K.

| Parameter | Value |
|---|---|
| Absorption coefficient (775 nm) $\alpha$[a] | $1.4\times10^4$ cm$^{-1}$ |
| Absorption coefficient (830 nm) $\alpha_p$[a] | $1.0\times10^4$ cm$^{-1}$ |
| Two-photon absorption coefficient (1550 nm) $\beta$[b] | $10^{-10}$ m/W |
| Free-carrier absorption cross section (1550 nm) $\sigma_e$[c] | $10^{-23}$ m$^{-2}$ |
| $(X,L)$-$\Gamma$ intervalley scattering rate $\gamma_{X,L}$[d] | (2.5 ps)$^{-1}$ |
| Electron momentum relaxation rate $\gamma_\Gamma$[e] | (125 fs)$^{-1}$ |
| Hole momentum relaxation rate $\gamma_{hh}$[f] | (60 fs)$^{-1}$ |
| Electron-hole scattering rate $\gamma_{\Gamma\text{-}hh}$[g] | $2.5\times10^6$ ms$^{-1}$ $(N_{\Gamma,hh})^{1/3}$ |
| Carrier cooling rate $\gamma_C$[g] | (500 fs)$^{-1}$ |

[a]Reference 22.
[b]Reference 33.
[c]Reference 20.
[d]Reference 23.
[e]Reference 34.
[f]Reference 35.
[g]Reference 1.

Rather, we adopt an approach similar to that used by others to describe high-field transport in semiconductors based on a displaced Maxwellian carrier distribution for electrons and holes.[30–32] For equilibrium conditions, the Maxwell or Boltzmann distribution approximation is valid for carrier densities $<4\times10^{17}$ cm$^{-3}$ for temperatures $>300$ K. Since the pulse focal spot size (~100 $\mu$m) in the experiments is much larger than the grating spacing $\Lambda_g$ (~2 $\mu$m), all variables are taken to be functions of only one spatial coordinate $x$, as considered in Sec. II above. As in the experiments, we take the sample to be 1 $\mu$m thick but neglect depth-dependent variation of injected carrier densities and currents. We do not distinguish between $L$ and $X$ valleys since neither is optically accessible by our probe beam and both valleys have similar effective masses and low mobility. Finally, we consider all injected holes to be heavy holes; in general, injected light holes quickly scatter into heavy-hole bands until their equilibrated population is $<5\%$ of that of the heavy holes.

*(i) Carrier population*. The continuity equation for carrier density evolution is

$$\frac{\partial N_c}{\partial t}+\frac{\partial(N_c u_c)}{\partial x}=\left.\frac{\partial N_c}{\partial t}\right|^S \tag{7}$$

for $c$=hh, $\Gamma$, and $(X,L)$. For holes, the source-sink term is $\partial N_{hh}/\partial t|^S=\{\alpha_{2\omega}(1-R)I^{2\omega}G(t)+\beta(1-R)^2[I^\omega G(t)]^2\}/2\hbar\omega$, where $I^{\omega,2\omega}$ are the incident peak intensities of $\omega,2\omega$ Gaussian pulses, $G(t)$, and $R=0.25$ is the GaAs reflectivity. The absorption coefficient and the values of other relevant parameters for GaAs are given in Table I. For $\Gamma$-valley electrons $\partial N_\Gamma/\partial t|^S=\partial N_{hh}/\partial t|^S-\{[\sigma_e N_\Gamma(1-R)I^\omega G(t)]/\hbar\omega\}+\gamma_{X,L}N_{X,L}$. The second term incorporates the transfer of electrons to $(X,L)$ valleys through free-carrier absorption with

absorption cross section $\sigma_e$. The third term represents $(X,L)$ electrons returning to the $\Gamma$ valley with the rate[23] $\gamma_{X,L}$. Finally, for $X,L$ electrons, $\partial N_{X,L}/\partial t|^s=\{[\sigma_e N_\Gamma(1-R)I^\omega G(t)]\}/\hbar\omega-\gamma_{X,L}N_{X,L}$. We neglect motion of the $(X,L)$ electrons, since this can only be induced by the space-charge field but their velocities are small due to their low mobility ($<5\%$ of the $\Gamma$ electrons[21,22]).

*(ii) Momentum density*. For holes and $\Gamma$ electrons moving within parabolic bands, the time evolution of the carrier momentum density, $P_c=N_c m_c^* u_c$, is expressed by

$$\frac{\partial P_c}{\partial t}+\frac{\partial}{\partial x}(u_c P_c)=\pm eN_c E(x,t)+\left.\frac{\partial P_c}{\partial t}\right|^S. \tag{8}$$

The first term on the right-hand side (RHS) represents the change via the space-charge field $E$ as defined by Poisson's equation [Eq. (4)]; the $(-)$ sign applies to electrons with the $(+)$ sign appropriate for holes. The effective dielectric constant $\varepsilon$ of the thin semiconductor, with air on one side and a low index dielectric substrate (glass), is taken to be $\sim 1/4$ of its bulk value of[21] $\sim 12$ due to image charge effects. While the particular value of $\varepsilon$ influences the amplitude of the density grating during the pulse, it does not substantially affect the pair grating amplitude that occurs with local charge neutrality by the end of the pump pulses (see below). The source-sink terms for holes and $\Gamma$ electrons incorporate velocity injection and decay: $\partial P_c/\partial t|^S=m_c^* u_c^s(\partial N_c/\partial t)|^{inj}-N_c m_c^*\gamma_c u_c \pm N_c m_\Gamma^*\gamma_{\Gamma-hh}(u_\Gamma-u_{hh})$. The first term relates to carrier injection at the swarm velocity, while the second term represents momentum relaxation with rate $\gamma_c$ due to carrier-phonon scattering and scattering of carriers with their own species.[34] The last term expresses momentum relaxation due to electron-hole scattering.[35]

While electrons can reasonably be associated with parabolic bands, heavy (and light) hole bands in GaAs are warped and nonparabolic in character. For example, near the band edge, the heavy hole effective mass varies between $0.35m_0$ and $0.6m_0$ for $\vec{k}$ between the [100] and [110] directions.[36] In GaAs, for light polarized along the [100] direction, the heavy-hole states that are preferentially excited have $\vec{k}$ directed near the [010] or $[0\bar{1}0]$ directions.[36] Quantum interference leads to a polar distribution of holes (and electrons) in $k$ space with the population of $(k_x,k_y,0)$ states differing from $(-k_x,k_y,0)$ states. A current is directed along [100], but the holes have a higher effective mass and lower group velocity than holes with the same energy but with different $\vec{k}$, e.g., near the [100] direction. Hence, once the holes are scattered from their initial $\vec{k}$ states, they respond with a lower effective mass to a developing space charge field, which opposes carrier motion along [100]. We emphasize that while crystal momentum $\hbar\vec{k}$ is conserved in the generation of each electron-hole pair, the holes are injected with a lower velocity along the [100] direction than they would be if the hole bands were isotropic and parabolic, with the average mobility effective mass $m_{hh}^*$. For parabolic bands, conservation of crystal momentum is equivalent to $m_{hh}^* u_{hh}^s+m_\Gamma^* u_\Gamma^s=0$ To incorporate the effect of band warping in the simulations, while retaining a one-dimensional (1D) model with constant, average effective mass involved in carrier transport, we take the initial (swarm) velocity of the heavy holes to be $u_{hh}^s=-0.9(m_\Gamma^*/m_{hh}^*)u_\Gamma^s$ with $m_{hh}=0.5m_0$.[22] This choice for the hole swarm velocity is consistent with that calculated from tensor elements[18] $\eta_c^{xxxx}$; for balanced carrier generation used in the simulations, the swarm velocities are approximately $u_\Gamma^s=-3\times10^5$ ms$^{-1}$ and $u_{hh}^s=3\times10^4$ ms$^{-1}$.

*(iii) Carrier temperature*. For our densities, carrier energy thermalization occurs within the conduction and hole bands faster than the momentum scattering time,[1,37] allowing us to define electron and hole temperatures and Boltzmann distribution functions. Indeed, as seen in the experimental results of Fig. 3, the rise time for the differential transmission of the probe beam, which is sensitive to electron states lower in energy than where electrons are injected, closely follows the pump pulse temporal profile so that thermalization must be occurring within the pump pulses' duration. Thermalization of carriers may be questionable early in the optical pump pulses when some of the carrier energy is contained in directed (hydrodynamic) motion and the carrier density is low, but by the time the pump pulses peak and the fraction of energy contained in directed motion is small, establishment of a common temperature for carriers is a reasonable approximation.[37] The common carrier temperature $(T_c=T_\Gamma)$ evolves according to

$$\frac{\partial T_\Gamma}{\partial t}=\left.\frac{\partial T_\Gamma}{\partial t}\right|^S, \tag{9}$$

where we ignore energy transport effects. The source-sink term for the electrons and/or holes is $\partial T_\Gamma/\partial t|^S=\{[(2\hbar\omega-E_g)/3k_B]-T_\Gamma\}N_\Gamma^{-1}\partial N_\Gamma/\partial t|^S-\gamma_C(T_\Gamma-300)$, where the excess photon energy is considered to be shared by an electron-hole pair and $\gamma_C$ is the carrier cooling rate. The cooling rate of $\Gamma$-valley electrons could be reduced by $(X,L)$ electrons bringing energy $\Delta_{X,L}$ energy back to the $\Gamma$ valley but since $N_{X,L}\ll N_\Gamma$, this effect is negligible.

Because a carrier density grating is formed during the pulse, under uniform pumping [ $(\partial N_\Gamma/\partial t)|^S$ does not vary with $x$], a temperature grating develops. As shown in the Appendix, this grating is estimated to have a peak amplitude of $\sim 2$ K. The contribution of such a temperature modulation to $f_\Gamma^{(1)}$, the occupancy grating amplitude [see Eq. (5)], for our probe wavelength is $\sim 10^{-4}$. This is comparable to the contribution to $f_\Gamma^{(1)}$ of the density grating at its peak; hence, while the temperature grating is weak, its contribution to grating diffraction is not negligible. For both grating types, from Eqs. (5) and (6), we find that the overall diffraction efficiency is estimated to be $\leqslant 10^{-9}$ for peak carrier densities similar to those obtained in the experiments. Such a low diffraction efficiency is consistent with the values found experimentally.

Figure 6 shows the time-dependent velocity grating amplitude $u_c^{(1)}$ of the heavy holes and $\Gamma$ electrons for $I^{2\omega}=25$ MW cm$^{-2}$ and $I^\omega=10$ GW cm$^{-2}$ and pulse width (FWHM) of 150 fs, as in the experiments; the total injected carrier density is $\sim 3\times10^{17}$ cm$^{-3}$ with each pulse generating half this density (balance condition). The quiescent carrier density of electrons and holes is taken to be $10^{14}$ cm$^{-3}$ at

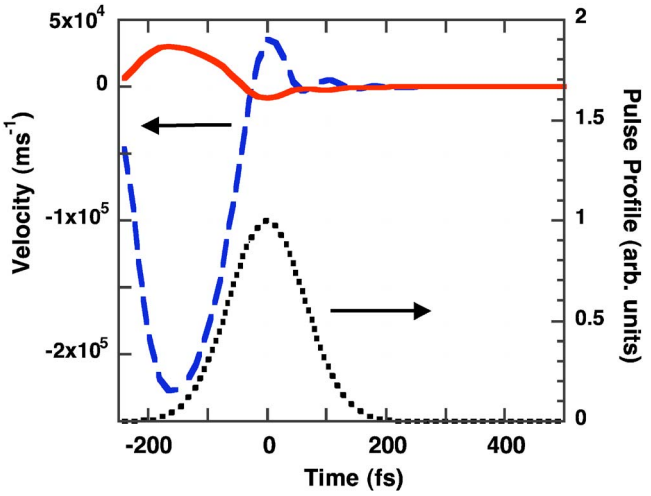


FIG. 6. (Color online) Simulated electron (dashed curve) and heavy hole (solid curve) velocities after injection of charge currents by 25 MW cm$^{-2}$, 775 nm and 10 GW cm$^{-2}$, 1550 nm pump pulses. The dotted curve indicates a pump pulse profile with 150 fs full width at half maximum.

300 K. Electrons and holes are injected in opposite directions and reach their maximum velocity (close to the swarm velocity) early in the optical pulse; the velocity decreases rapidly due to momentum relaxation and space-charge effects, with the latter inducing plasma oscillations. As suggested earlier,[38] the carriers, in response to space-charge and damping effects, undergo motion similar to that of a damped harmonic oscillator. Strong scattering between electrons and holes damps this motion.

The hole population follows the integral of the pump pulses' temporal profile before reaching its peak value of $3 \times 10^{17}$ cm$^{-3}$. The $\Gamma$-valley population also increases rapidly during the pump pulse and more slowly thereafter as a small number ($\sim$5% of the total) of electrons transfer back from the $(L,X)$ valleys. Figure 7 shows the evolution of the $\Gamma$-electron and hole grating amplitudes, $N_{\Gamma}^{(1)}$ and $N_{\mathrm{hh}}^{(1)}$, as well

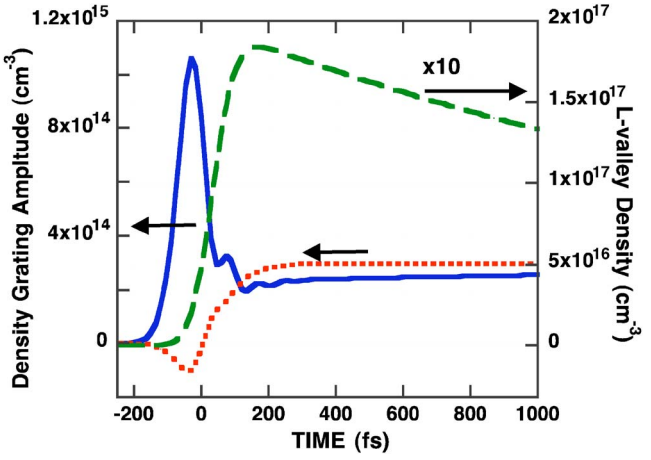


FIG. 7. (Color online) Simulated $L$-valley electron density $N_L^{(0)}$, (large dashes), heavy-hole density grating amplitude $N_{\mathrm{hh}}^{(1)}$ (dots), and $\Gamma$-valley grating amplitude $N_{\Gamma}^{(1)}$ (solid curve) as a function of time for the same pumping parameters used for Fig. 6.

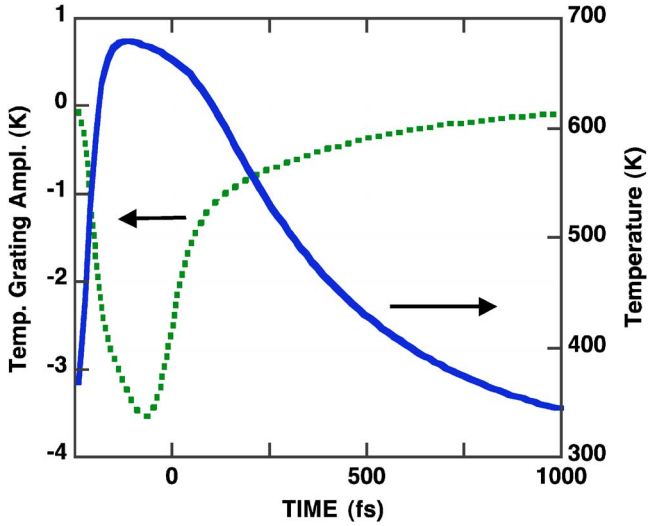


FIG. 8. (Color online) Simulated electron-hole temperature (solid curve), and carrier temperature grating amplitude (dotted curve) $T_{\Gamma}^{(1)}$ as a function of time for same pumping parameters used in Fig. 6.

as the population of electrons in $(X,L)$ valleys. Both grating amplitudes reach their maximum values near the peak of the pump pulses and then decay thereafter. By the end of the pump pulses, dielectric relaxation brings about charge neutrality but still leaves a pair grating with amplitude determined by hole band warping (see below). The grating amplitude $N_{\Gamma}^{(1)}$ reaches a maximum value that is $\sim$1% of the injected carrier density and evolves to the same value as $N_{\mathrm{hh}}^{(1)}$, after the $(L,X)$ electrons return. The peak value $[N_{\Gamma}^{(1)}/N_{\Gamma}^{(0)}]_{peak}=-K_g u_{\Gamma}^s/\gamma_{\Gamma}$ (see the Appendix) is essentially the product of the electron displacement during quasiballistic motion ($\sim$30 nm) and the grating wave vector. Electrons promoted to $(X,L)$ valleys by free-carrier absorption during pumping make up the part of the density grating, but do not contribute to the probe diffraction efficiency, which is only sensitive to occupancy in the $\Gamma$ valley. When the $(X,L)$ electrons return, they increase the diffraction for $t>1$ ps. At lower pump intensities, the role of free-carrier absorption is reduced and the $(L,X)$ electrons play less of a role in defining the grating diffraction efficiency.

Figure 8 shows the simulated spatially averaged carrier temperature $T_{\Gamma}^{(0)}$ and the temperature grating amplitude $T_{\Gamma}^{(1)}$ as a function of time. As expected, the average temperature indicates cooling to the lattice temperature on a 500 fs time scale. The negative value of $T_{\Gamma}^{(1)}$ in Fig. 8 is consistent with Eq. (A7) if a positive density grating is formed. $|T_{\Gamma}^{(1)}|$ has its maximum value ($\sim$2 K) just after the peak of the pump pulses, a value, which can also be easily estimated from the transport equations (see the Appendix). The temperature grating amplitude subsequently decays along with the overall carrier temperature due to cooling.

### D. Discussion

Figure 9 shows the time-dependent simulated grating efficiency $\zeta$ at 830 nm for $I^{2\omega}\sim 5$ MW cm$^{-2}$ and $I^{\omega}$

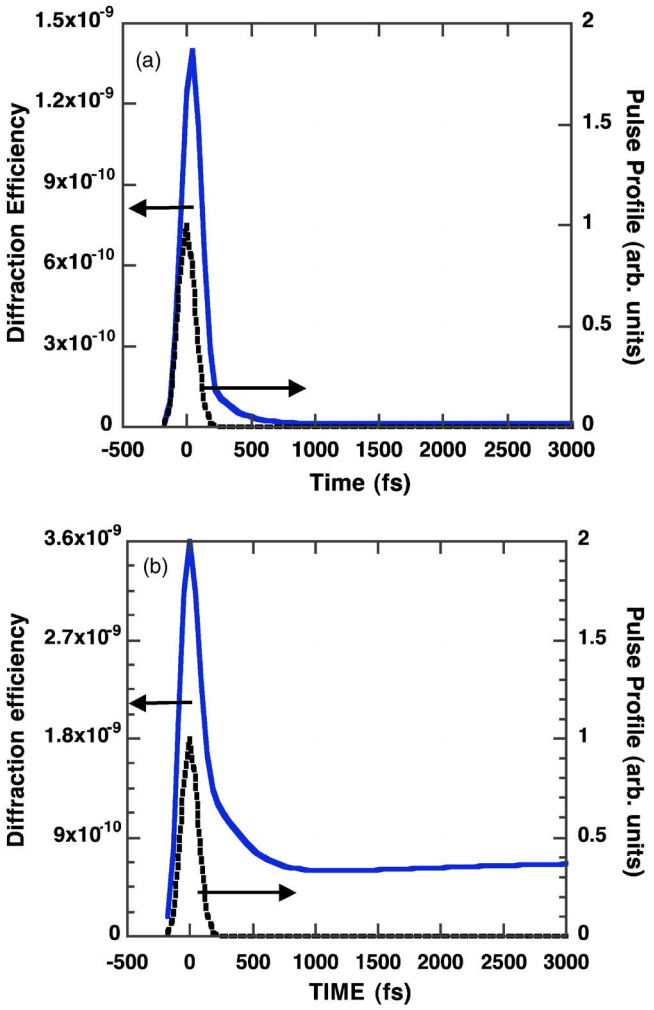


FIG. 9. (Color online) Simulated grating diffraction efficiency $\zeta$ as a function of time (solid curve) for (a) 5 MW cm$^{-2}$, 775 nm and 5 GW cm$^{-2}$, 1550 nm pump pulses and (b) parameters of Fig. 6 (solid curve). A pump pulse profile (dashed curve) with 150 fs FWHM is also shown.

$\sim$4GW cm$^{-2}$ and for $I^{2\omega} \sim 25$ MW cm$^{-2}$ and $I^{\omega} \sim 10$ GW cm$^{-2}$. Near the peak of the pump pulse, $\zeta$ is large because of the highly transient charge density and temperature gratings, which interfere constructively. The peak value we observe for the higher pumping condition is $\sim 3 \times 10^{-9}$, in surprisingly good agreement with the experimental value recorded for the highest intensity pump beams (Fig. 4), and also justifying the choice of swarm velocities or the values of injection current tensor elements. The peak of the diffraction efficiency near zero time delay is temporally shifted (especially for the lower intensity pump pulses) from zero time delay. The effect is more noticeable for lower pump intensities, but the simulation results are not as large as those observed experimentally (Fig. 4), likely due to our assumption of density-independent, instantaneous carrier thermalization. Weak modulation in $\zeta$ with a period of $\sim$100 fs is indicative of plasma oscillations.[38] These are not observable in the experimental results of Fig. 4, such as due to temporal convolution effects between pump and probe beams. Following the generation process (i.e., for $t$=0.1–1 ps), a decay in $\zeta$ is evident both in the simulation and the experiment (Fig. 3). The 500 fs decay time constant can be traced to the decay of the temperature grating amplitude $T_{\Gamma}^{(1)}$ through Eq. (5). The first term on the RHS (related to density) is always positive (being the product of two positive terms), and for an 830 nm probe the second term (product of $T_{\Gamma}^{(1)}$ and $\partial f_{\Gamma}/\partial T$, both of which are negative for temperatures well above 300 K) is also positive. Cooling effects therefore reduce the magnitude of $T_{\Gamma}^{(1)}$ producing a *decrease* in $\zeta$. Note that under the same pumping conditions, cooling produces an increase in differential transmission ($\Delta T/T$) (Fig. 3) since $\Delta T/T \propto \alpha_0[N_{\Gamma}^{(0)} \partial f_{\Gamma}/\partial N_{\Gamma} + (T_{\Gamma}^{(0)} - 300)\partial f_{\Gamma}/\partial T_{\Gamma}]$. The density contribution increases and becomes positive during optical pumping and the return of $(X,L)$ electrons, while the temperature contribution is negative *after* the pulse, and with cooling tends to zero for our probe wavelength.

The appearance of a pair grating is evident in Fig. 9 at $t > 1$ ps, by which time space-charge effects and carrier cooling are essentially complete. For the higher pump intensities, intervalley transfer is also evident in the next few picoseconds. Although $N_{X,L} \ll N_{\Gamma}$, because the $(L,X)$ electron grating amplitude is formed by free-carrier absorption during the pump pulse when (see Fig. 7) the $N_{\Gamma}^{(1)}$ grating amplitude is largest, and because the electrons are relatively immobile in the $(L,X)$ valleys, their influence on the pair grating amplitude is significant.

It is not *a priori* obvious that a pair grating should form following the ballistic and drift motion of the carriers, since it might be thought that dielectric relaxation would render the carrier system spatially homogenous. However, as discussed earlier, its origins can be traced to band warping for the holes. Indeed, if band warping is not included in our model and momentum conservation is strictly observed within a parabolic band model, no pair grating is obtained [apart from the much weaker effect associated with $(X,L)$ electrons]. Because carrier-lattice collisions also do not conserve momentum within the carrier systems, this type of momentum transfer can also lead to a pair grating. However, for our parameters, the diffraction efficiency for such a grating is $<10^{-12}$. By combining and integrating the density and velocity equations for the carriers (see the Appendix), we find that after ballistic and drift motions have ceased, the amplitude of the pair grating is given approximately by

$$N_{\Gamma,\mathrm{hh}}^{(1)} \approx -\frac{K_g N_{\Gamma,\mathrm{hh}}^{inj} P^{inj}}{\sum_{c=\Gamma,\mathrm{hh}} m_c^* \gamma_c}, \tag{10}$$

where $P^{inj} = m_{\Gamma}^* u_{\Gamma}^s + m_{\mathrm{hh}}^* u_{\mathrm{hh}}^s < 0$ is a measure of the hole band warping and $N_{\Gamma,\mathrm{hh}}^{inj}$ is the total injected electron or hole density. Space-charge fields, as seen above, influence the carrier dynamics, governing the population grating behavior during optical excitation, determining when charge neutrality occurs, etc., but within the approximations used here, *do not influence the pair grating amplitude*. For the parameters considered here, $N_{\Gamma,\mathrm{hh}}^{(1)} < 10^{-3} N_{\Gamma,\mathrm{hh}}^{(0)}$, more than an order of magnitude smaller (see Fig. 7) than the peak value of $N_{\Gamma}^{(1)}$ (i.e., during optical pumping). The grating efficiency shown in Fig. 9 corresponds to $P^{inj} < 0$. If $P^{inj} > 0$, the grating effi-

ciency would have dropped to zero just after the pump pulse and then increased; this is not observed experimentally.

The returning electrons increase the grating efficiency by ~20%, while the experimental results of Figs. 3(b) and 3(c) indicate an increase in the diffraction efficiency larger than this. Part of this difference is related to the much higher carrier densities obtained in the experiments, for which Boltzmann statistics are not appropriate. A more quantitative comparison might also have to take into account the fact that the free-carrier absorption cross section during the optical pulse is higher than the value at 300 K assumed here, and pump-probe Pauli blocking factors are more significant in the experiments. Pump saturation effects are also not considered in the simulations. Overall, the comparison of Figs. 4 and 9 shows qualitatively similar features. From the overall low magnitude of the calculated $\zeta$, one can also understand why the measured grating efficiencies is so small and has such low signal to noise.

Finally, it is worth emphasizing that while pair grating generation is well known to occur via the *classical* interference of single-color beams incident at noncollinear angles on a semiconductor,[3] we demonstrate here that such a grating can also occur following current generation via quantum interference effects. Direct carrier density control is also possible via quantum interference of two color beams in connection with a $\chi^{(2)}$ nonlinear optical process.[39] As shown elsewhere,[40] when noncollinear beams are used, a pair grating is formed via this $\chi^{(2)}$ process and, for certain polarization combinations, this grating interferes with the one produced by a current grating. It is also worth noting that the generation of a density grating in a semiconductor via classical interference does not generally lead to a temperature grating as well since, unlike the quantum interference case, the peak intensity in the classical case is also spatially modulated.

Figure 10 shows the simulated $\zeta$ at its peak value ($t \sim 0$), where a charge and/ or temperature grating has formed, and at $t=4$ ps, where the pair grating remains; these are shown as a function of $I^{2\omega}$, with $I^{\omega}$ adjusted for balanced carrier generation. The maximum intensities are those associated with peak carrier density of $3\times10^{17}$ cm$^{-3}$. At low intensities, the dependence of $\zeta$ on $I^{2\omega}$ at $t \sim 0$ is linear, consistent with the data in Fig. 5. The deviation from linearity relates mainly to space-charge dynamics with a small contribution coming from the density dependence of the electron-hole scattering time (as verified by making the latter density independent). With increasing carrier density, both mechanisms increasingly restrict the maximum velocity that the carriers can attain and therefore the amplitude of the electron and hole population gratings; this in turn, restricts the amplitude of the electron-hole temperature grating that can form since that grating depends on a modulation in the electron density. The sublinear behavior is consistent with the data in Fig. 5. Pump saturation effects may also be playing a role in the experiments. The experimental and simulated values of $\zeta$ at $t=4$ ps are determined by the pair density grating amplitude. At very low intensities where free-carrier absorption of 1550 nm photons, space-charge fields are negligible, $\zeta$ should depend quadratically on $I^{2\omega}$, and indeed this occurs in the simulations. Because the experimental diffraction efficiency is so weak at the lower pump intensities, within limitations of signal to noise it is difficult to determine if the quadratic behavior is observed experimentally. At higher intensities, the experimental diffraction efficiency appears to vary linearly with intensity. The deviation from quadratic behavior likely reflects details (e.g., pump saturation, Fermi-Dirac statistics, etc.) not included in the simple model.

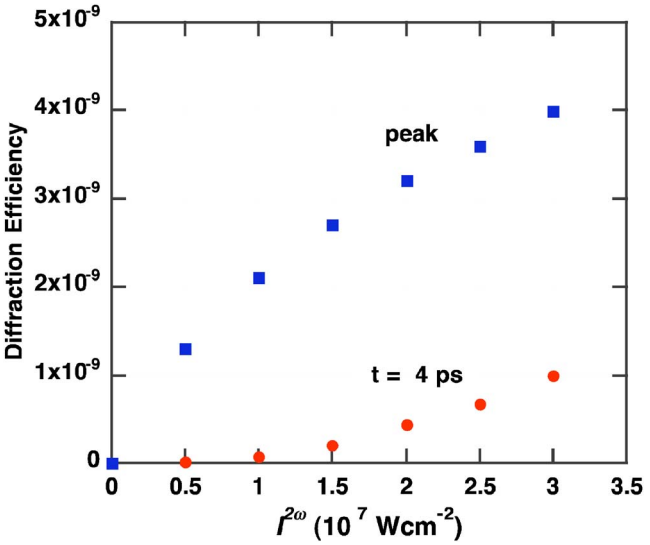


FIG. 10. (Color online) Simulated diffraction efficiency $\zeta$ as a function of $I^{2\omega}$ with $I^{\omega}$ adjusted so that an equal density of carriers is generated by single- and two-photon absorption. The $\zeta$ is shown at the diffraction peak ($t \sim 0$ ps) (squares) and at $t=4$ ps (circles).

## IV. CONCLUSIONS

In summary, we have produced transient charge current gratings through quantum interference between one- and two-photon absorptions of ~150 fs, 775 and 1550 nm pulses, noncollinearly incident on GaAs at room temperature, and have studied the subsequent carrier evolution. The experiments allow the observation of carrier dynamics during a transition from ballistic to drift to diffusive motion. Several features are observed from these unusual current gratings, whose evolution is probed using 830 nm, 150 fs pulses. The current gratings lead to charge density, carrier temperature, and eventually electron-hole pair, population gratings. A simple model using known GaAs parameters is developed to qualitatively interpret the complex grating dynamics. The charge-density grating whose amplitude is ~1% of the injected density forms with the electrons displaced by ~30 nm following ballistic injection. The grating largely decays by the end of the pump pulses through momentum relaxation and space-charge effects. A carrier temperature grating with amplitude of ~1 K contributes strongly to the diffraction efficiency until it decays by carrier cooling in ~500 fs. Over the next several picoseconds, the pair grating grows as it is reinforced by carriers returning from the $(L,X)$ conduction bands to which electrons are transferred by free-carrier absorption during optical pumping. This effect becomes more noticeable at higher pump intensities for which

interband absorption saturates and space-charge fields restrict the Γ-valley electron population, but they do not restrict free carrier absorption. The pair density grating decays by ambipolar diffusion and carrier recombination on a 15 ps time scale. Finally, the coherent control current injection process exposes the nonparabolic nature and anisotropy of the hole bands, allowing neutral electron-hole pair gratings to be generated.

The model we have used is simple, given the highly nonequilibrium nature of the carriers generated, and is only intended to provide qualitative insight. At this level, it appears to explain several features of the data, such as the appearance of charge and pair gratings as well as temperature gratings. The use of coherence control of current gratings has therefore led to the observation of several physical phenomena not observable with other techniques for electronic or optical excitation of semiconductors. The grating techniques in combination with a more systematic study as well as a more detailed model incorporating detailed $k$-space dynamics and many-body effects[41] might therefore provide insights into properties of nonequilibrium carrier distributions. While the above results for carrier displacement are obtained using a grating geometry, the spatially dependent carrier temperature and population distributions might also be observable, and indeed aspects have already been observed,[4] with tightly focused beams in which carriers are displaced to opposite sides of an excitation region.

## ACKNOWLEDGMENTS

The authors gratefully acknowledge stimulating discussions with A. Najmaie, J. E. Sipe, and E. Sherman. This work was supported in part by the Natural Sciences and Engineering Research Council of Canada, Photonics Research Ontario, the Defense Advanced Research Projects Agency, and the Office of Naval Research.

## APPENDIX A: ESTIMATES OF GRATING AMPLITUDES

From the expansions in Eq. (4), the first-order diffraction amplitude can be obtained by considering only the coefficients of those terms containing $\cos K_g x$. If we neglect the side valley scattering, the first-order density and velocity grating amplitudes for electrons or heavy holes are related by

$$\frac{\partial N_c^{(1)}}{\partial t} + K_g N_c^{(0)} u_c^{(1)} = 0. \tag{A1}$$

From Eq. (8), the grating amplitudes of carrier density and velocity are related by

$$\frac{\partial (N_c^{(0)} m_c^* u_c^{(1)})}{\partial t} = \pm \frac{e}{K_g \varepsilon} N_c^{(0)} (N_{\rm hh}^{(1)} - N_\Gamma^{(1)}) - N_c^{(0)} \gamma_c m_c^* u_c^{(1)} \pm N_c^{(0)} \gamma_{\Gamma-h} m_c^* (u_\Gamma^{(1)} - u_{\rm hh}^{(1)}) + \left. m_c^* u_c^s \frac{\partial N_c^{(0)}}{\partial t} \right|^{inj}. \tag{A2}$$

Adding these equations for electrons and holes gives

$$\frac{\partial}{\partial t}\left( \sum_c N_c^{(0)} m_c^* u_c^{(1)} \right) = -\sum_c m_c^* \gamma_c u_c^{(1)} + \sum_c m_c^* u_c^s \left. \frac{\partial N_c^{(0)}}{\partial t} \right|^{inj} = \frac{1}{K_g} \sum_c m_c^* \gamma_c \frac{dN_c^{(1)}}{dt} + \sum_c m_c^* u_c^s \left. \frac{\partial N_c^{(0)}}{\partial t} \right|^{inj}. \tag{A3}$$

When Eq. (A3) is integrated from the beginning of the optical pulse until charge neutrality occurs and the ballistic velocities return to near zero, we have

$$0 = \frac{N_\Gamma^{(1)}}{K_g} (m_\Gamma^* \gamma_\Gamma + m_{\rm hh}^* \gamma_{\rm hh}) + N_{\Gamma,h}^{inj} (m_\Gamma^* u_\Gamma^s + m_{\rm hh}^* u_{\rm hh}^s), \tag{A4}$$

where $m_\Gamma^* u_\Gamma^s + m_{\rm hh}^* u_{\rm hh}^s$ is a measure of band warping or nonparabolicity of the hole band and is zero for parabolic bands. Since the electron and heavy-hole density grating amplitudes are the same for charge neutrality, we have that the pair grating amplitude is

$$N_{\Gamma,{\rm hh}}^{(1)} \approx -K_g \frac{(m_\Gamma^* u_\Gamma^s + m_{\rm hh}^* u_{\rm hh}^s) N_{\Gamma,{\rm hh}}^{inj}}{m_\Gamma^* \gamma_\Gamma + m_{\rm hh}^* \gamma_{\rm hh}}. \tag{A5}$$

For our parameters $N_{\Gamma,{\rm hh}}^{(1)} / N_{\Gamma,{\rm hh}}^{inj} \sim 10^{-3}$. As noted in the text, at high intensities interband processes involving $(L,X)$ valleys also contribute to the density grating amplitudes after $\sim 1$ ps.

One can also estimate the peak grating amplitude of the electron density grating (near the peak of the pulse) by integrating Eq. (A1) to give $(N_\Gamma^{(1)})_{peak} = -K_g \int N_\Gamma^{(0)} u_\Gamma^{(1)} dt \approx -K_g (N_\Gamma^{(0)})_{peak} u_\Gamma^s / \gamma_\Gamma$ if the momentum relaxation time is taken to be short compared to the pulse width. This gives $[N_\Gamma^{(1)} / N_\Gamma^{(0)}]_{peak} = -K_g u_\Gamma^s / \gamma_\Gamma$, which for our parameters is $\sim 10^{-2}$. Similarly, the peak hole density grating $(N_{\rm hh}^{(1)} / N_{\rm hh}^{(0)})_{peak} \approx -K_g u_{\rm hh}^s / \gamma_{\rm hh}$, which for our parameters is $\sim -10^{-3}$.

In the case of temperature effects, we see that a grating expansion of Eq. (9) yields

$$\frac{\partial T_\Gamma^{(1)}}{\partial t} = \frac{-N_\Gamma^{(1)}}{(N_\Gamma^{(0)})^2} \left( \frac{2\hbar\omega - E_g}{3k_B} - T_\Gamma^{(0)} \right) \left. \frac{\partial N_\Gamma}{\partial t} \right|^S - \gamma_C T_\Gamma^{(1)}. \tag{A6}$$

Hence, one sees that the temperature grating depends on energy density in the presence of an electron density grating, essentially a specific heat effect, and forms only in the presence of some cooling, which makes the term in brackets nonzero. An estimate of the peak temperature grating amplitude can be obtained by taking $\partial T_\Gamma^{(1)} / \partial t = 0$, $\partial N_\Gamma / \partial t|^S = (N_\Gamma^{(0)}) / \tau_p$, where $\tau_p$ is the pulse width so that

$$(T_\Gamma^{(1)})_{peak} = \frac{1}{\tau_p \gamma_C} \left| \frac{N_\Gamma^{(1)}}{N_\Gamma^{(0)}} \right|_{peak} \left( \frac{2\hbar\omega - E_g}{3k_B} - T_\Gamma^{(0)} \right). \tag{A7}$$

For $[(2\hbar\omega - E_g)]/3k_B - T_\Gamma^{(0)} \approx 100$ K, $(T_\Gamma^{(1)})_{peak} \approx -1$ K.

*Email address: vandriel@physics.utoronto.ca

[1] J. Shah, *Ultrafast Spectroscopy of Semiconductors and Semiconductor Nanostructures*, 2nd ed. (Springer, New York, 1999).
[2] B. S. Wherret, A. L. Smirl, and T. F. Boggess, IEEE J. Quantum Electron. **QE-19**, 680 (1983); J.-L. Oudar, A. Migus, D. Hulin, G. Grillon, J. Etchepare, and A. Antonetti, Phys. Rev. Lett. **53**, 384 (1984).
[3] *Optical Phase Conjugation*, edited by R. A. Fisher (Academic, New York, 1983); B. I. Sturman and V. M. Fridkin, *The Photovoltaic and Photorefractive Effects in Noncentrosymmetric Materials* (Gordon and Breach, Philadelphia, 1992); A. L. Smirl, G. C. Valley, K. M. Bohnert, and T. F. Boggess, Jr., IEEE J. Quantum Electron. **24**, 289 (1988).
[4] R. Atanasov, A. Haché, J. L. P. Hughes, H. M. van Driel, and J. E. Sipe, Phys. Rev. Lett. **76**, 1703 (1996); A. Hache, Y. Kostoulas, R. Atanasov, J. L. P. Hughes, J. E. Sipe, and H. M. van Driel, *ibid.* **78**, 306 (1997); M. J. Stevens, A. L. Smirl, R. D. R. Bhat, J. E. Sipe, and H. M. van Driel, J. Appl. Phys. **91**, 4382 (2002).
[5] A. Haché, J. E. Sipe, and H. M. van Driel, IEEE J. Quantum Electron. **34**, 1144 (1998).
[6] N. Laman, A. I. Shkrebtii, J. E. Sipe, and H. M. van Driel, Appl. Phys. Lett. **75**, 2581 (1999); M. Bieler, N. Laman, H. M. van Driel, and A. L. Smirl, *ibid.* **86**, 061102 (2005).
[7] M. Sheik-Bahae, Phys. Rev. B **60**, R11257 (1999).
[8] T. M. Fortier, P. A. Roos, D. J. Jones, S. T. Cundiff, R. D. R. Bhat, and J. E. Sipe, Phys. Rev. Lett. **92**, 147403 (2004).
[9] R. D. R. Bhat and J. E. Sipe, Phys. Rev. Lett. **85**, 5432 (2000); M. J. Stevens, A. L. Smirl, R. D. R. Bhat, A. Najmaie, J. E. Sipe, and H. M. van Driel, *ibid.* **90**, 136603 (2003); J. Hübner, W. W. Rühle, M. Klude, D. Hommel, R. D. R. Bhat, J. E. Sipe, and H. M. van Driel, *ibid.* **90**, 216601 (2003).
[10] R. D. R. Bhat, F. Nastos, A. Najmaie, and J. E. Sipe, Phys. Rev. Lett. **94**, 096603 (2005); H. Zhao, X. Pan, A. L. Smirl, R. D. R. Bhat, A. Najmaie, J. E. Sipe, and H. M. van Driel, Phys. Rev. B **72**, 201302(R) (2005).
[11] E. Dupont, P. B. Corkum, H. C. Liu, M. Buchanan, and Z. R. Wasilewski, Phys. Rev. Lett. **74**, 3596 (1995).
[12] D. H. Marti, M. A. Dupertuis, and B. Deveaud, Phys. Rev. B **69**, 035335 (2004); **72**, 075357 (2005).
[13] S. D. Ganichev, E. L. Ivchenko, V. V. Bel'kov, S. A. Tarasenko, M. Sollinger, D. Weiss, W. Wegscheider, and W. Prettl, Nature (London) **417**, 153 (2002).
[14] H. T. Duc, T. Meier, and S. W. Koch, Phys. Rev. Lett. **95**, 086606 (2005).
[15] M. V. Éntin, Sov. Phys. Semicond. **23**, 664 (1989).
[16] E. A. Manykin and A. M. Afanas'ev, Sov. Phys. JETP **25**, 828 (1967) [Zh. Eksp. Teor. Fiz. **52**, 1246 (1967)]; P. Brumer and M. Shapiro, Acc. Chem. Res. **22**, 407 (1989); P. Brumer and M. Shapiro, Sci. Am. **272** (3), 34 (1995).
[17] Y. Kerachian, P. Nemec, H. M. van Driel, and A. L. Smirl, J. Appl. Phys. **96**, 430 (2004).
[18] R. D. R. Bhat and J. E. Sipe (unpublished).
[19] K. Seeger, *Semiconductor Physics*, Springer Series in Solid State Sciences Vol. 40, 4th ed. (Springer, New York, 1989), p. 133.
[20] W. G. Spitzer and J. M. Whelan, Phys. Rev. **114**, 59 (1959).
[21] O. Madelung, *Semiconductors: Basic Data* (Springer, Berlin, 1996).
[22] J. S. Blakemore, J. Appl. Phys. **53**, R123 (1982).
[23] J. Shah, B. Deveaud, T. C. Damen, W. T. Tsang, A. C. Gossard, and P. Lugli, Phys. Rev. Lett. **59**, 2222 (1987); S. Zollner, S. Goplan, and M. Cardona, J. Appl. Phys. **68**, 1682 (1990); D. Y. Oberli, J. Shah, and T. C. Damen, Phys. Rev. B **40**, 1323 (1989).
[24] P. Langot, R. Tommasi, and F. Vallée, Phys. Rev. B **54**, 1775 (1996).
[25] B. A. Bennet, R. A. Soref, and J. A. Del Alamo, IEEE J. Quantum Electron. **26**, 113 (1990).
[26] A. Yariv and P. Yeh, *Optical Waves in Crystals* (Wiley, New York, 1984).
[27] H. M. van Driel, Phys. Rev. B **19**, 5928 (1979); J. H. Collet, A. Cornet, M. Pugnet, and T. Amand, Solid State Commun. **42**, 883 (1982); W. Pötz and P. Kocevar, Phys. Rev. B **28**, 7040 (1983).
[28] J. F. Young and H. M. van Driel, Phys. Rev. B **26**, 2147 (1982).
[29] H. Haug and S. W. Koch, *Quantum Theory of the Optical and Electronic Properties of Semiconductors* (World Scientific, Singapore, 2004); W. Schäfer and M. Wegener, *Semiconductor Optics and Transport Phenomena* (Springer, New York, 2002); R. Binder and S. W. Koch, Prog. Quantum Electron. **19**, 307 (1995).
[30] K. Huang, *Statistical Mechanics* (Wiley, New York, 1963).
[31] E. M. Conwell, *High Field Transport in Semiconductors* (Academic, New York, 1967).
[32] K. Bløtekjår, IEEE Trans. Electron Devices **ED-17**, 38 (1970).
[33] M. D. Dvorak, W. A. Schroeder, D. R. Andersen, A. L. Smirl, and B. S. Wherrett, IEEE J. Quantum Electron. **30**, 256 (1994); D. C. Hutchings and B. S. Wherrett, Phys. Rev. B **49**, 2418 (1994).
[34] A. Dargys and J. Kundrotas, *Handbook on Physical Properties of Ge, Si, GaAs and InP* (Science and Encyclopedia, Vilnius, 1994); E. Kuphal, A. Schlachtezki, and A. Pöcker, Appl. Phys. **1**, 520 (1978); J. Y. D. Wiley, in *Mobility of Holes in III-V Compounds in Semiconductors and Semimetals*, edited by R. K. Willardson and A. C. Beer (Academic, New York, 1975).
[35] R. A. Höpfel, J. Shah, P. A. Wolff, and A. C. Gossard, Phys. Rev. B **37**, 6941 (1988).
[36] M. Cardona and P. Yu, *Fundamentals of Semiconductors* (Springer, New York, 1996).
[37] D. W. Snoke, W. W. Rühle, Y.-C. Lu, and E. Bauser, Phys. Rev. B **45**, 10979 (1992).
[38] H. M. van Driel, Chem. Phys. **251**, 309 (2000).
[39] J. M. Fraser, A. I. Shkrebtii, J. E. Sipe, and H. M. van Driel, Phys. Rev. Lett. **83**, 4192 (1999).
[40] Y. Kerachian, H. M. van Driel, and A. L. Smirl, following paper, Phys. Rev. B **75**, 125206 (2007).
[41] H. T. Duc, Q. T. Vu, T. Meier, H. Haug, and S. W. Koch, Phys. Rev. B **74**, 165328 (2006).